International Journal of Fracture **115:** 101–123, 2002.

Delamination buckling and propagation analysis of honeycomb panels using a cohesive element approach

TONG-SEOK HAN[1,*], ANI URAL[1], CHUIN-SHAN CHEN[2], ALAN T. ZEHNDER[3], ANTHONY R. INGRAFFEA[1] and SARAH L. BILLINGTON[4]
[1]*Cornell Fracture Group, Frank Rhodes Hall, Cornell University, Ithaca, NY 14853, U.S.A. (*Author for correspondence; E-mail: han@stout.cfg.cornell.edu)*
[2]*Computer-Aided Engineering, Department of Civil Engineering, National Taiwan University, Taipei, Taiwan*
[3]*Department of Theoretical and Applied Mechanics, Cornell University, Ithaca, NY 14853, U.S.A.*
[4]*School of Civil and Environmental Engineering, Cornell University, Ithaca, NY 14853, U.S.A.*

Received 18 April 2001; accepted in revised form 29 January 2002

Abstract. The cohesive element approach is proposed as a tool for simulating delamination propagation between a facesheet and a core in a honeycomb core composite panel. To determine the critical energy release rate (G_c) of the cohesive model, Double Cantilever Beam (DCB) fracture tests were performed. The peak strength (σ_c) of the cohesive model was determined from Flatwise Tension (FWT) tests. The DCB coupon test was simulated using the measured fracture parameters, and sensitivity studies on the parameters for the cohesive model of the interface element were performed. The cohesive model determined from DCB tests was then applied to a full-scale, 914×914 mm (36×36 in.) debond panel under edge compression loading, and results were compared with an experiment. It is concluded that the cohesive element approach can predict delamination propagation of a honeycomb panel with reasonable accuracy.

Key words: Buckling, cohesive crack model, delamination propagation, finite element analysis, Honeycomb composite panels, interface element.

1. Introduction

A High-Speed Civil Transport (HSCT) has been proposed as a next generation supersonic commercial aircraft (Williams, 1995; Wilhite and Shaw, 1997). Realization of the aircraft has been faced with numerous environmental, economic, and technical challenges. One of the technical challenges has been the development of an airframe with light-weight, stiff and damage-tolerant structural materials, since the aircraft must withstand severe loading conditions and high temperature (about 177 °C (350 °F)) during a supersonic cruise (Miller et al., 1998).

A solution for weight reduction is honeycomb core sandwich panel construction (Figure 1). The high stiffness/weight ratio of the panel is obtained by using a light weight core to connect composite laminate facesheets. However, little is known regarding the damage tolerance of such panels not only under normal service loading conditions but also under the unexpected severe loading conditions they may encounter. Manufacturing defects, in-service mechanical loading conditions, and entrapped water in the honeycomb core under thermo-cyclic loading can cause debonding between a facesheet and the honeycomb core. The existing debond may lead to catastrophic delamination propagation which will eventually cause failure of the structural member.

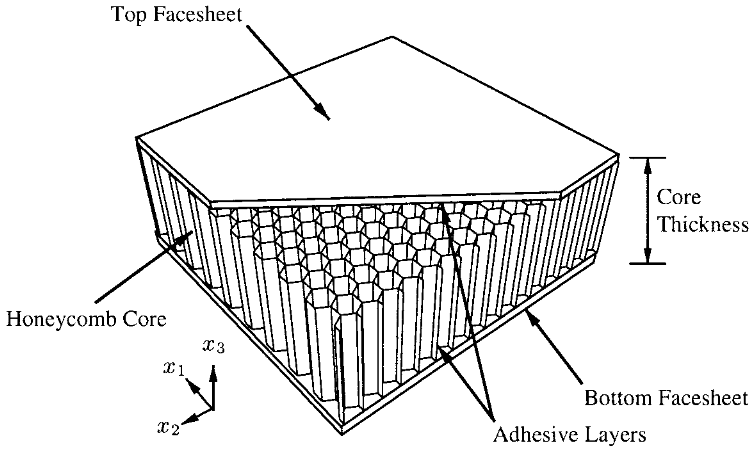

Figure 1. Honeycomb sandwich panel.

Broad research has been done in the damage tolerance of composite materials. Chai et al. (1981) investigated buckling and post-buckling behavior; energy release rates were calculated to predict delamination propagation load for the two dimensional case. Two dimensional delamination buckling and growth in a honeycomb panel due to in-plane loading was examined by Kim et al. (1981). Interfacial crack growth in composite plates was investigated by Nilsson and Storakers (1992). A buckling induced delamination growth analysis (Nilsson et al., 1993) and a stability analysis (Nilsson and Giannakopoulos, 1995) of the delamination propagation using perturbation method were performed. Using shell elements, Klug et al. (1996) applied the crack closure method to predict the delamination propagation and stability of a delaminated composite plate. Whitcomb (1981) used the three dimensional finite element approach to characterize the buckling and post-buckling behavior of homogeneous quasi-isotropic materials for through-width delamination, and later for embedded delamination (Whitcomb, 1989). He investigated the strain energy release rate along a crack front to predict delamination propagation. The effect of a contact zone was also examined (Whitcomb, 1992). Most of these previous analyses decouple the interaction between structural behavior and the fracture process, and thus can only used as a first order approximation for damage tolerance assessment. One way to couple the structural behavior and the fracture process is to use a cohesive zone model. The model was introduced to investigate the fracture process with nonlinear fracture mechanics (Barenblatt, 1962; Dugdale, 1960). It has been noted that, combined with the finite element method, the cohesive zone model approach can simulate the crack propagation of various types of problems (de Andres et al., 1999; Ortiz and Pandolfi, 1999).

The objective of this work was to provide and to verify a computational tool for simulating delamination buckling and propagation in a honeycomb panel that can be extended to panels with fairly complicated geometry. In order to simulate the buckling-driven delamination propagation process, a computational nonlinear fracture mechanics approach was adopted. Specifically, the cohesive crack approach combined with the finite element method was used to simulate the delamination propagation.

The cohesive crack approach or cohesive zone approach is characterized by interface elements with a cohesive constitutive model. As shown in Figure 2, the interface elements are inserted between the facesheet and honeycomb core for geometrical representation of

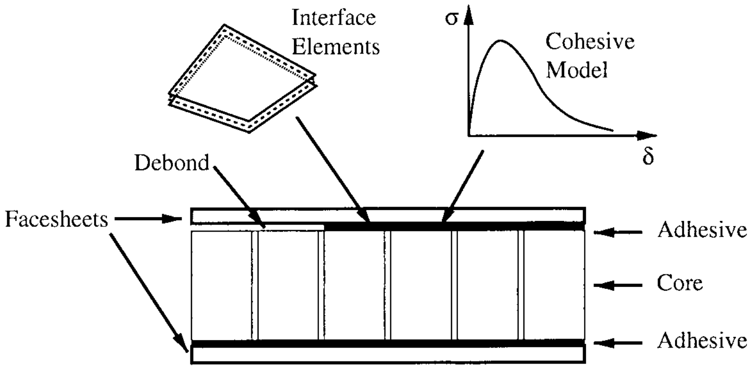

Figure 2. Modeling of honeycomb panel.

the adhesive and the debonding process, and the cohesive constitutive model is applied to reproduce traction-separation behavior between the facesheet and core. The idea of using the cohesive approach is to include a complex behavior around the crack front between the facesheet and the core into the simple cohesive model for crack propagation analysis. To our best knowledge, application of the cohesive element model to a honeycomb sandwich panel subject to buckling-driven delamination propagation has not been reported in the literature. Thus, it is our goal to provide a systematic approach to using the cohesive model, determined from coupon tests, to predict full-scale response. Numerical studies using various material parameters of the cohesive model are carried out to assess the predictive sensitivities of structural damage tolerance.

In the following, the computational methodology pursued in this study is outlined. The delamination propagation problem was investigated using a honeycomb panel composed of 24-ply polymer-matrix composite facesheets and a graphite composite honeycomb core which has 4.76 mm (3/16 in.) hexagon cells. Double Cantilever Beam (DCB) and Flatwise Tension (FWT) tests were performed, and the fracture parameters for the cohesive model were obtained. Using these parameters, the DCB test was simulated. As a more realistic case, a 914×914 mm (36×36 in.) panel under edge compression loading, and with an initial facesheet debond (305×457 mm (12×18 in.)), was investigated. The facesheet buckling and delamination propagation in the debond panel were simulated, and the results were compared with those from an experiment. The performance of the cohesive model approach as a computational tool for simulating the delamination propagation in a honeycomb panel is discussed.

2. Computational methodology

The cohesive crack model proposed by Dugdale (1960) and Barenblatt (1962) is applied to simulate the debond propagation. The cohesive crack model is characterized by a traction-separation law, which is a function of the fracture energy and the strength of the interface (Figure 3). According to Griffith theory, singular stresses are predicted at a crack front. However, the cohesive crack model results in a non-singular stress at a crack front. If the cohesive zone ahead of the crack front is very small compared to other geometric dimensions of the problem, the Griffith and the cohesive crack models are equal in their prediction of fracture behavior (Rice, 1968).

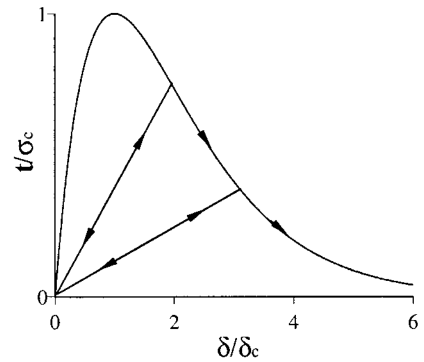

Figure 3. Cohesive traction separation model (t: effective traction, δ: effective displacement, σ_c/δ_c: critical (peak) effective traction/effective displacement at peak traction).

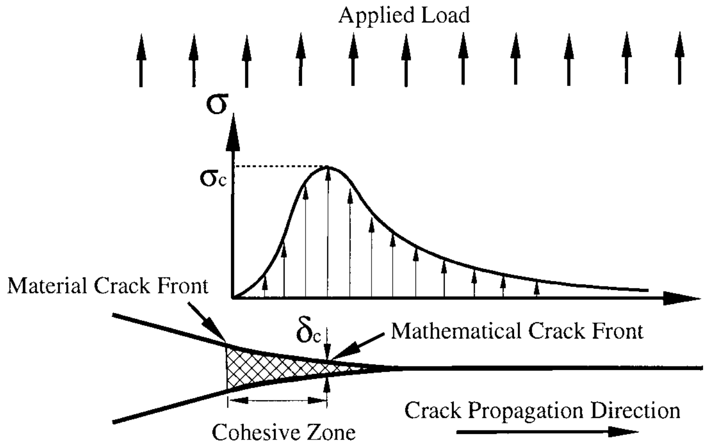

Figure 4. Cohesive crack model around crack front.

The tensile stress distribution on the new cracked surface is illustrated in Figure 4 which represents a crack front at the adhesive layer with a debond in Figure 2. A true or material crack front is a point where the stress is zero after softening. A fictitious or mathematical crack front is defined as a point where the maximum stress occurs along the interface. The cohesive or fracture process zone is the region between the true crack front and the mathematical crack front. All the complicated fracture process including debonding of the adhesive and delamination between plies in a facesheet is included in the cohesive fracture model.

An interface element approach (de Andres et al., 1999; Ortiz and Pandolfi, 1999) is used to model the cohesive crack propagation as opposed to a mixed boundary condition approach (Wei and Hutchinson, 1997). The interface element is a zero-thickness element which is a degenerate form of a continuum element. Unlike the continuum element, the constitutive model for the interface element is formulated with a relation between traction (t) and relative displacements (δ) along the interface. In this work, an eight-noded 3-D interface element is used as shown in Figure 5. The cohesive constitutive model for the interface element is based on the formulation of Ortiz and Pandolfi (1999), and takes the form:

$$\mathbf{t} = \frac{\partial \phi}{\partial \delta_n}(\delta_n, \delta_S, \mathbf{q})\mathbf{n} + \frac{\partial \phi}{\partial \delta_S}(\delta_n, \delta_S, \mathbf{q})\frac{\boldsymbol{\delta}_S}{\delta_S} = t_n\mathbf{n} + t_S\frac{\boldsymbol{\delta}_S}{\delta_S}, \tag{1}$$

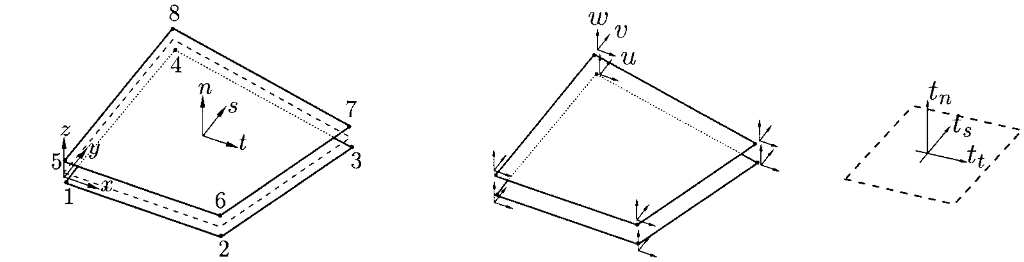

a. 3D eight-noded interface element b. Displacements and tractions

Figure 5. Schematic of interface element.

where subscript n represents a component on the n axis, and subscript S represents the resultant shear component from the t and s directions. Also, $\mathbf{t}$ is a traction at an integration point of an interface element, ϕ is the Helmholtz free potential, $\mathbf{n}$ is a unit normal of the interface element, δ_n is the relative displacement in the normal direction, δ_S is the relative displacement resultant in the shear direction ($\delta_S = \sqrt{\delta_t^2 + \delta_s^2}$), $\boldsymbol{\delta}_S/\delta_S$ is a unit vector in the direction of shear relative displacement resultant, and $\mathbf{q}$ is a vector of collected internal state variables. Traction t_n is a normal component of traction vector $\mathbf{t}$ as shown in Figure 5b, and t_S is the resultant of shear tractions t_t and t_s ($t_S = \sqrt{t_t^2 + t_s^2}$).

The effective opening displacement defined for simple coupling of the normal and shear modes is:

$$\delta = \sqrt{\delta_n^2 + \beta^2 \delta_S^2} \tag{2}$$

where β represents the contribution of the shear mode to the fracture process ($0 \leq \beta \leq 1$). If we further assume that 50% of the shear displacement contributes to the effective opening displacement, β reduces to $1/\sqrt{2}$. Then, the effective traction can be shown to be (Ortiz and Pandolfi, 1999):

$$t = \sqrt{t_n^2 + \beta^{-2} t_S^2}. \tag{3}$$

The Helmholtz free potential is selected as:

$$\phi = e\sigma_c\delta_c \left[1 - \left(1 + \frac{\delta}{\delta_c} \right) e^{-\delta/\delta_c} \right], \tag{4}$$

from which the fracture energy (G_c) can be expressed as:

$$G_c = \lim_{\delta \to \infty} \phi = e\sigma_c\delta_c. \tag{5}$$

Assuming secant unloading/reloading (Figure 3), the relationship between the effective traction and effective displacement becomes:

$$t = \begin{cases} e\sigma_c \dfrac{\delta}{\delta_c} e^{-\delta/\delta_c} & \text{if } \delta = \delta_{\max} \text{ and } \dot{\delta} \geq 0, \\ \dfrac{t_{\max}}{\delta_{\max}} \delta & \text{if } \delta < \delta_{\max} \text{ or } \dot{\delta} < 0, \end{cases} \tag{6}$$

where σ_c and δ_c are the stress and displacement at the peak of the cohesive model shown in Figure 3, and $t_{\max}$ and $\delta_{\max}$ are the maximum effective traction and relative displacement throughout a loading history. In compression, a simple linear elastic behavior with a very high stiffness is assumed to model the contact between the facesheet and the core. This stress-softening, mode-coupled cohesive model was implemented via a user-supplied subroutine in a commercial finite element code.

3. Double cantilever beam (DCB) simulation

The ultimate objective of the current research is to apply the cohesive model to a realistic structure so one can simulate facesheet buckling and delamination propagation. However, a simpler problem was investigated first to understand the fundamental behavior of the delamination process and to determine the cohesive model. This was achieved by performing DCB experiments and by accurately simulating the experiments based on fracture parameters obtained from the experiments. The calibrated model was then applied to a realistic structure (a 914×914 mm (36×36 in.) debond panel) as described in Section 4.

The facesheets of the honeycomb panel are composed of a 24-ply fiber-reinforced polymer-matrix composite (PMC, IM7/5260 grade 145 tape). The facesheets sandwich a 25.4 mm (1 in.) thick HFT-G (graphite) honeycomb core. The stacking sequence of the 24-ply facesheet is $[45/-45/90/0/45/-45/90/0/45/-45/90/0]_s$, which makes it quasi-isotropic. Applied load (P) versus crack length (a) from the DCB simulation results are compared with experimental results. The DCB specimens were cut from undamaged regions of the 914×914 mm (36×36 in.) debond panel.

3.1. Experiment

To characterize the fracture process between the facesheet and the honeycomb core and to determine the fracture parameters for the cohesive model, DCB (Figure 6) and FWT (Figure 7) tests were performed (Ural et al., 2001). The FWT test data were used to determine σ_c of the cohesive model for the interface element. Four 24-ply DCB specimens were tested to measure G_c for the cohesive model, two for each bag and tool side of the honeycomb panel. The dimensions of the DCB specimens were 50.8×203×25.4 mm (2×8×1 in.) with a 50.8 mm (2 in.) pre-crack. Since the initial debond in the 914×914 mm (36×36 in.) panel was on the bag side, the results from the bag side DCB test were compared with computational simulation results. The G_c of the bag side was measured as 788 J/m^2 (4.5 lb/in.).

3.2. Modeling

For computational efficiency, all the nonlinearities were assumed to occur within the cohesive element along the interface between the facesheet and homogenized honeycomb core. The facesheets and the honeycomb core were modeled as linear elastic materials. The fracture process was modeled with the hyper-elastic, secant unloading/reloading constitutive model in interface elements as described in Section 2.

3.2.1. *Facesheets*

The facesheets were modeled with four-noded isotropic shell elements. The equivalent elastic modulus of the facesheet was extracted from the bending stiffness value, which was calculated using composite laminate theory (Tsai, 1987). This value was compared with the measured

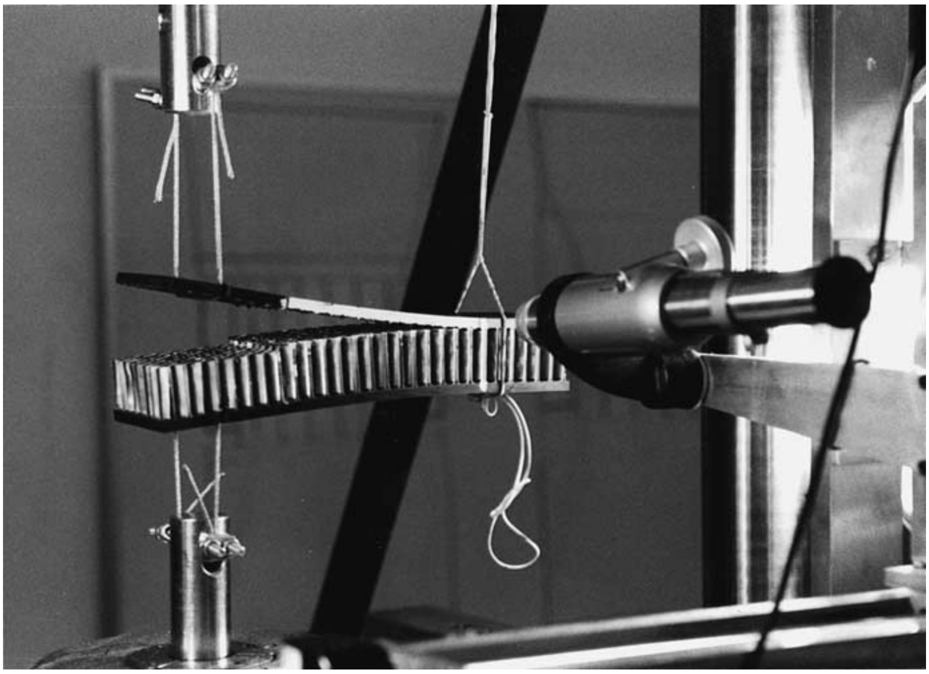

Figure 6. Honeycomb DCB experiment.

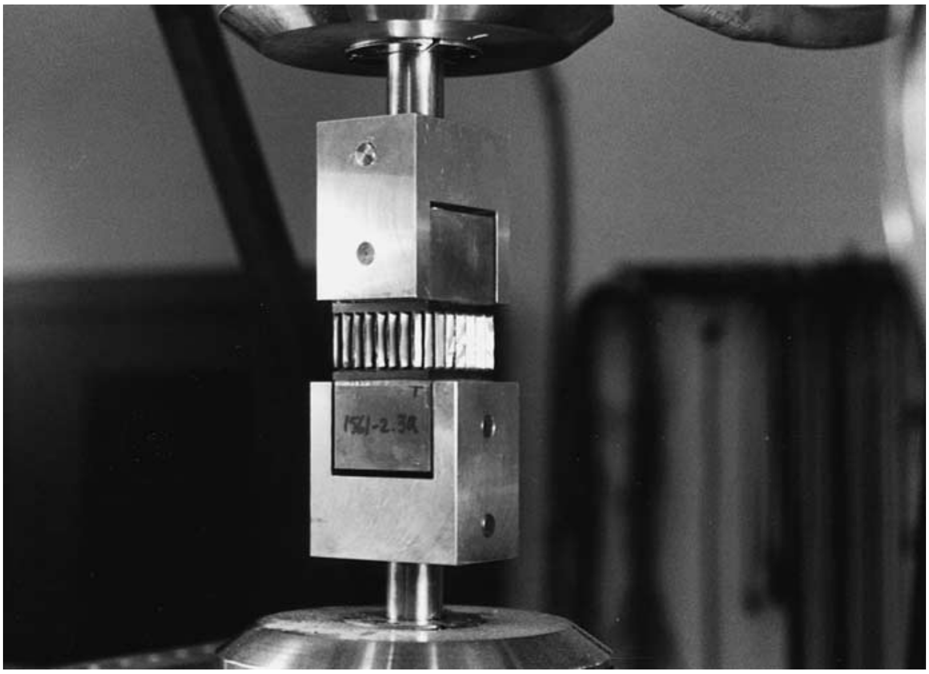

Figure 7. Honeycomb FWT experiment.

Table 1. Material properties for facesheets

Property	Magnitude
E	54.4 GPa (7890 ksi)[a] / 52.1 GPa (7560 ksi)[b]
ν	0.33
Density	1580 kg/m^3 (0.057 lb/in.^{3})
Thickness (24 layers)	3.30 mm (0.13 in.)

[a]Laminate theory.
[b]Measured from 3-point bending test (Ural et al., 2001).

Table 2. Material properties for homogenized honeycomb core

Property	Magnitude
E_1	689 kPa (0.1 ksi)
E_2	689 kPa (0.1 ksi)
E_3	888 MPa (128.8 ksi)
G_{12}	68.9 kPa (0.01 ksi)
G_{13}	1.47 GPa (212.75 ksi)
G_{23}	555 MPa (80.5 ksi)
ν_{12}	0.99
ν_{13}	0.00
ν_{23}	0.00
Density	96.0 kg/m^3 (6 lb/ft^3)
Thickness	25.4 mm (1 in.)

value from three point bending tests, Table 1 (Ural et al., 2001). The bending stiffness rather than the axial stiffness was selected because the delamination buckling and growth of the facesheet was dominated by the bending stiffness. Laminate theory predicted the elastic modulus with reasonable accuracy for the 24-ply facesheet. The equivalent elastic modulus of the facesheet from laminate theory was 4.4% larger than the measured elastic modulus (Table 1).

3.2.2. *Honeycomb core*

To reduce computational effort, eight-noded solid elements were used for the honeycomb core according to the core homogenization method proposed by Burton and Noor (1997).

As shown in Table 2, the honeycomb core properties have strong orthotropy. It should be noted that the in-plane ($x_1 - x_2$ plane, Figure 1) properties are much lower than the out-of-plane (planes in the x_3 direction) properties since the cell walls can easily bend in the $x_1 - x_2$ plane. Fairly small values of the in-plane properties compared with the out-of-plane properties were chosen since in-plane properties have little effect on the behavior of the honeycomb panel. However, care must be taken in selecting the in-plane properties in order to maintain the positive definiteness of the constitutive model of the homogenized core (Burton and Noor, 1997).

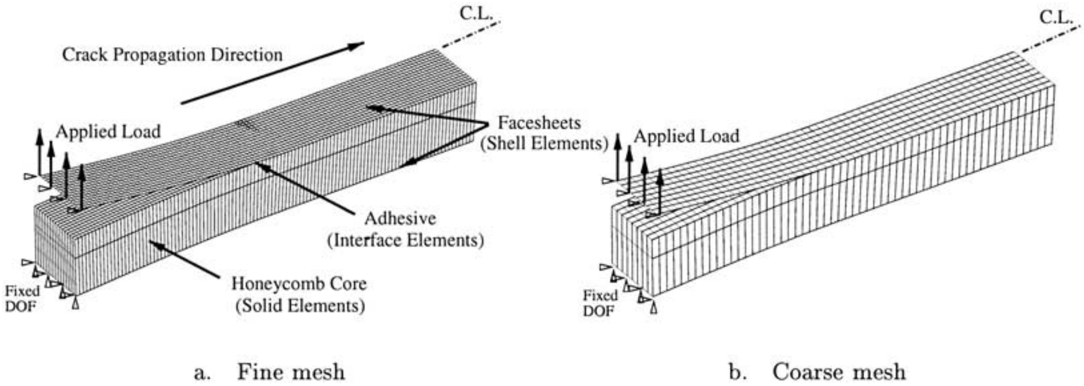

Figure 8. Finite element meshes for DCB simulation.

3.2.3. *Adhesive*

The adhesive was modeled using eight-noded interface elements with the cohesive model. The cohesive model for the interface element can be characterized by two parameters, the peak strength (σ_c) and the critical energy release rate (G_c) since the shape of the traction versus relative displacement is defined in Equation 6 from the Helmholtz potential shown in Equation 4. Then, the peak displacement (δ_c) can be automatically determined from the two parameters (σ_c, G_c) and Equation 5. The value of $G_c = 788$ J/m^2 (4.5 lb/in.) obtained from the DCB test was used. The σ_c can be determined from the FWT. Since the FWT test data for the honeycomb panel with the composite core were not available, the σ_c was selected from the FWT data for titanium core honeycomb panels (Ural et al., 2001). It is likely that the FWT results from the titanium and the composite core will not be different by more than a factor of two. Therefore, the average value of the FWT data for the titanium core, approximately 13.8 MPa (2000 psi), was used and is considered as a reasonable estimate. It should be noted that the FWT strength, 13.8 MPa (2000 psi), is based on the homogenized core, and the actual contact stress between the facesheet and the honeycomb core wall is 309 MPa (44800 psi). A sensitivity study on σ_c was performed to validate this assumption. Parametric studies on G_c and mesh size were also performed.

3.2.4. *Finite element mesh and solution strategy*

Two finite element meshes were created for different mesh sizes of the interface elements. The dimension of the DCB finite element meshes was $25.4\times178\times25.4$ mm ($1\times7\times1$ in.) with a 25.4 mm (1 in.) pre-crack. Only the half of the specimen was modeled using symmetry. The finite element mesh shown in Figure 8b has an interface element four times larger than that in the mesh shown in Figure 8a. The number of elements and degrees of freedom are compared in Table 3. Results from two finite element meshes are compared in Section 3.4.

Interface elements with a large elastic stiffness should be used with care due to oscillation in computed traction profiles. In order to avoid numerical divergence problems, Lobatto 3×3 numerical integration was used for the interface elements (Schellekens and de Borst, 1993).

To overcome the numerical divergence problems due to snap-through or snap-back behavior, a modified version of the arc-length control was applied. Specifically, the indirect displacement or crack mouth opening displacement (CMOD) control was used for DCB simulations. The normal relative displacements in the interface elements along the initial crack front were selected as parameters for the CMOD control solution process.

Table 3. Problem size comparison of two meshes.

Category	Fine mesh	Coarse mesh
Size of interface element[a]	1.59 mm (0.0625 in.)	3.18 mm (0.125 in.)
Number of shell/solid elements	3584	896
Number of interface elements	1535	384
Number of degrees of freedom	30 736	8208

[a]Dimension of square element

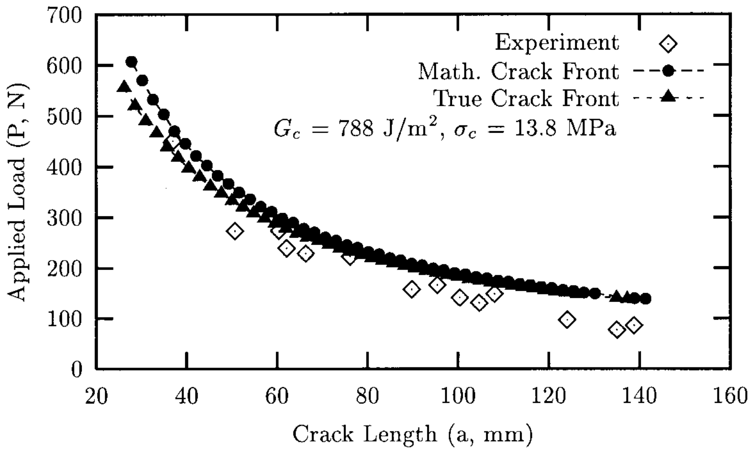

Figure 9. Comparison of applied load versus crack length.

3.3. Results

Simulation results using the fine mesh (Figure 8a) and experimental results from the 24-ply bag side DCB specimen are compared. The applied load (P) versus crack length (a) relationships are shown in Figure 9. The deformed shapes at four different crack lengths are shown in Figure 10. The simulation results predicted the experimental results reasonably well. Applied loads at a given crack length from the computational results were 10 to 30% higher than the experimental results between crack lengths of 50.8 mm (2 in.) to 102 mm (4 in.). It is noted that the experimental data within the first 25.4 mm (1 in.) should not be considered for comparison due to the effects of the initial sawcut pre-crack in the specimens. Also, the experimental data after a 102 mm (4 in.) crack length, where the edge-boundary conditions control the experiment, should not be taken into account.

3.4. Sensitivity

Sensitivity analyses to σ_c and G_c of the cohesive model and to the mesh size were performed for the DCB test.

3.5. Sensitivity to σ_c

Since σ_c of the cohesive model was selected based on the nominal stress from the FWT test for a titanium core, results of analyses with different σ_c values were compared. In Figure 11, the results for $\sigma_c = 13.8$ MPa (2000 psi), $G_c = 788$ J/m^2 (4.5 lb/in.) (Case 1) are plotted

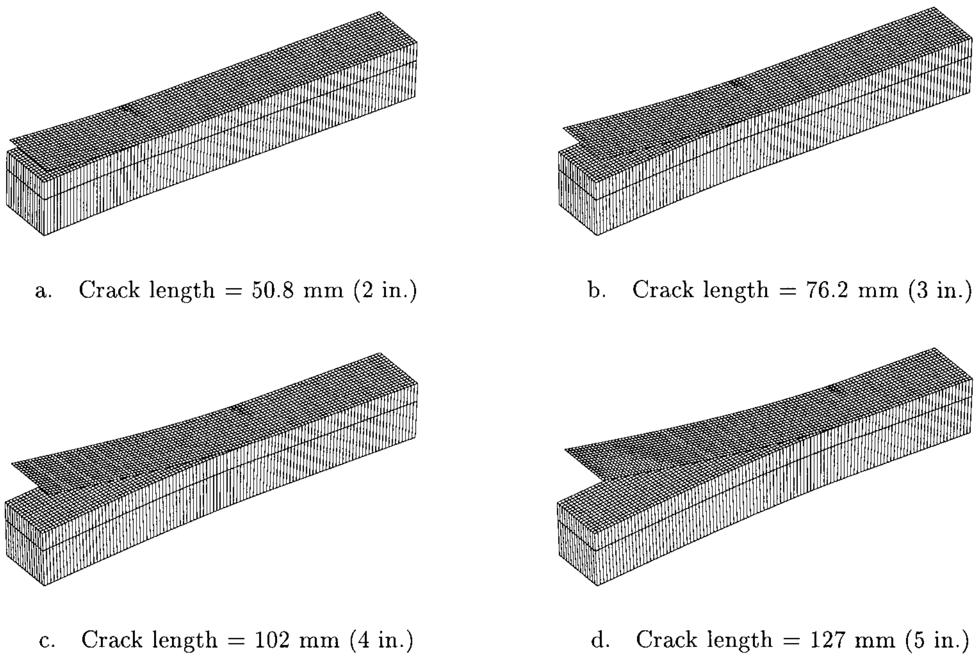

Figure 10. Deformed shape of DCB during delamination propagation (magnification factor for deformed shape = 1).

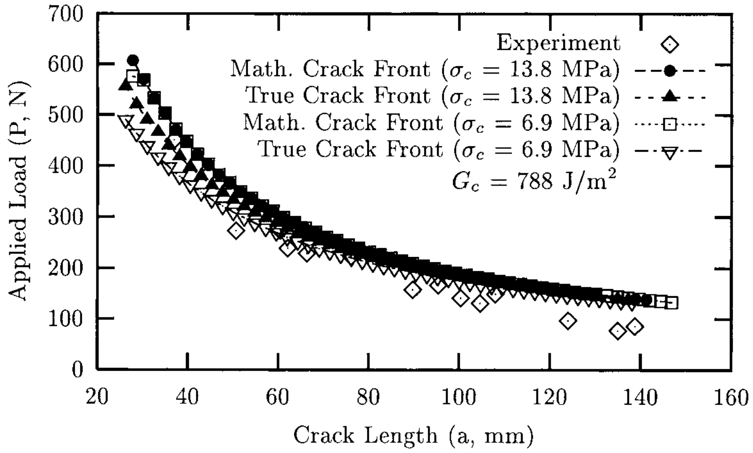

Figure 11. Sensitivity to σ_c (G_c = 788 J/m^2 (4.5 lb/in.)).

along with the results for $\sigma_c = 6.9$ MPa (1000 psi), $G_c = 788$ J/m^2 (4.5 lb/in.) (Case 2). The value of 6.9 MPa (1000 psi) for σ_c was selected since this value was considered as a lower bound.

From the simulations, we observed that the main difference between the two cases was the resulting length of the cohesive zone, the distance between true and mathematical crack fronts. The cohesive zone length for Case 2 was twice that of Case 1. However, the mathematical crack front path remained the same when σ_c was changed. The true crack front moved closer to the mathematical crack front with decrease of cohesive zone size (or increase of σ_c). This implies that the applied load is equilibrated by the local cohesive stresses around the same

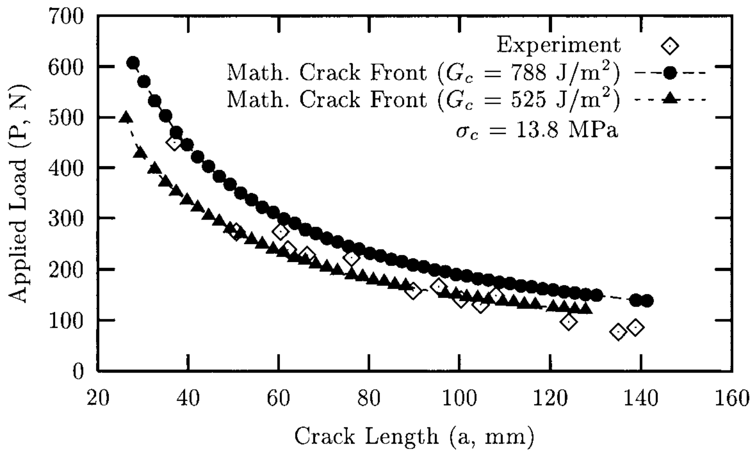

Figure 12. Sensitivity to G_c.

mathematical crack front as long as G_c remains the same. It is concluded that delamination propagation is not very sensitive to σ_c when G_c remains constant. It should be noted that the delamination initiation load before stress softening was influenced by σ_c. However, the influence was relatively small since the delamination load was increased by only 7% when σ_c was increased by 100% from 6.9 MPa (1000 psi) to 13.8 MPa (2000 psi) while G_c was kept constant.

3.6. Sensitivity to G_c

An analysis with 33% lower G_c was performed since the predicted applied loads were 10–30% higher than the experimental results. In Figure 12, it is shown that G_c is a sensitive parameter to reduce the critical load (P) at a given crack length (a). The 33% reduction of G_c caused about a 20% reduction in the load, which is a significant change when compared with the effect of changing σ_c. This also implies that the fracture mechanics-based approach is more reasonable than the strength-based approach for simulating the DCB specimen as also described in Cui and Wisnom (1993). Analyses results for $\sigma_c = 6.9$ MPa (1000 psi) and $\sigma_c = 13.8$ MPa (2000 psi) at $G_c = 525$ J/m^2 (3.0 lb/in.) are shown in Figure 13, and the same trend was also predicted as for $G_c = 788$ J/m^2 (4.5 b/in.).

3.7. Sensitivity to mesh size

A parametric study on the influence of mesh size on the results was performed. The simulation results, applied load (P) versus crack length (a), are compared in Figure 14 and Figure 15. Although the models with the larger mesh size predicted slightly larger cohesive zones, the overall behavior was the same. Thus, the mesh size of 3.18×3.18 mm (0.125×0.125 in.) was used for the 914×914 mm (36×36 in.) debond panel simulation to reduce the computational cost.

4. Debond panel simulation

Based on the results from the DCB simulation, the cohesive model was applied to a more realistic structure, a 914×914 mm (36×36 in.) debond panel under edge compression.

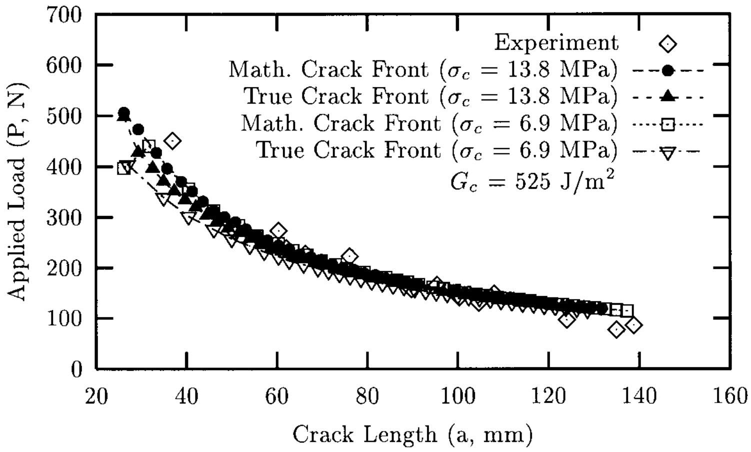

Figure 13. Sensitivity to σ_c (G_c = 525 J/m^2 (3.0 lb/in.)).

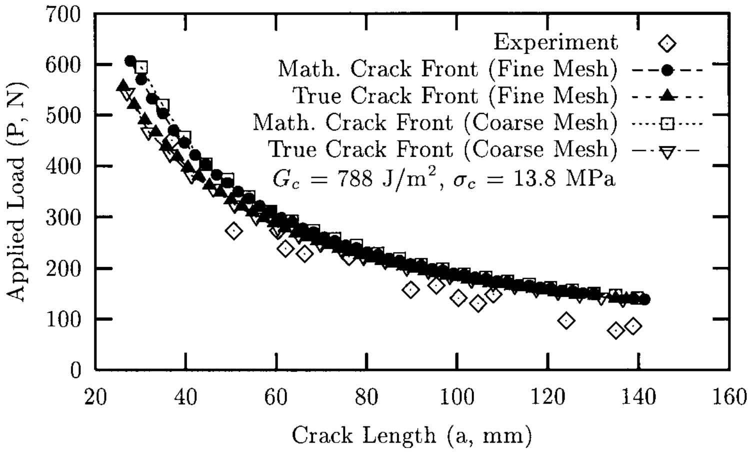

Figure 14. Sensitivity to mesh size (σ_c = 13.8 MPa (2000 psi)).

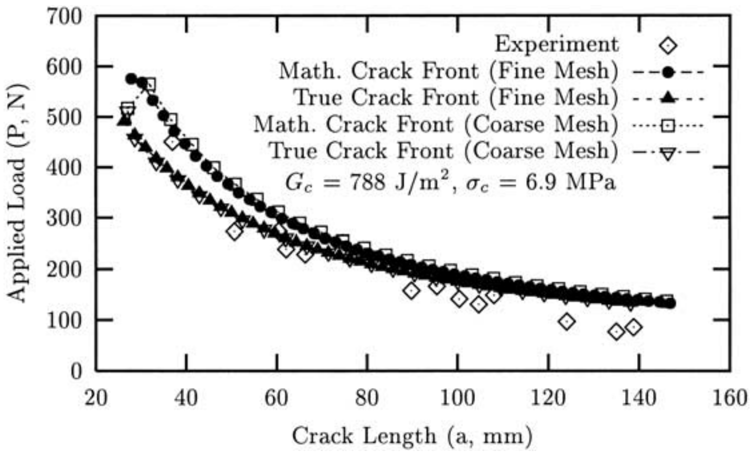

Figure 15. Sensitivity to mesh size (σ_c = 6.9 MPa (1000 psi)).

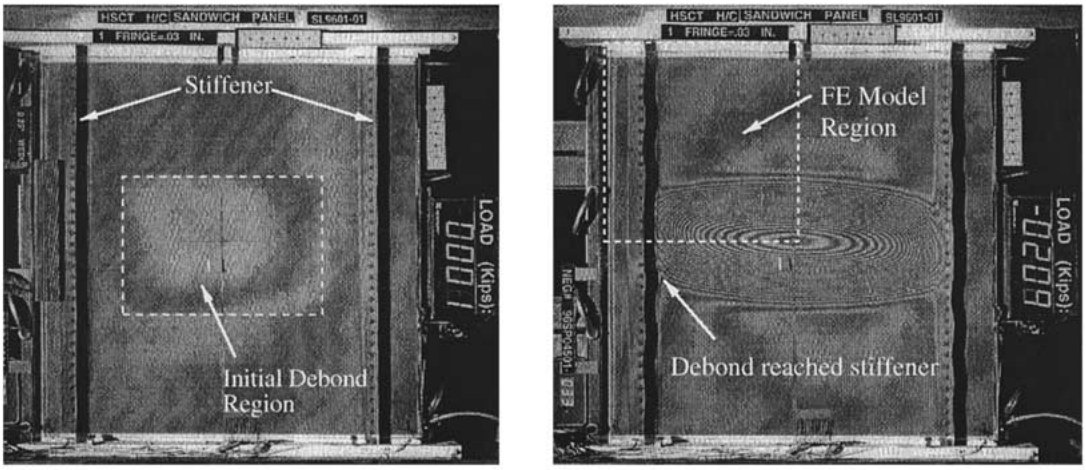

a. **Before delamination propagation** b. **After delamination propagation**

Figure 16. Honeycomb debond panel experiment (shadow moiré fringe patterns in (b) depict the out-of-plane displacements of the facesheet due to the facesheet buckling and delamination propagation (Boeing, 96).)

4.1. Experiment

The experiment, performed at Boeing, consisted of a 914×914 mm (36×36 in.) square sandwich panel with an initial, centrally-located debond between the bag side of the facesheet and the composite honeycomb core (Figure 16). The dimension of the debond was 305×457 mm (12×18 in.), longer in the horizontal direction. The panel was loaded in edge compression in the ribbon direction (vertical direction in Figure 16, and x_1 direction in Figure 1). More details on the experiment can be found in Boeing (1996).

The total propagation length from the initial debond front to the stiffeners was 95.3 mm (3.75 in.). Crack growth was initially stable, but it became unstable and very fast propagation was observed. The fast crack propagation was retarded when the crack front reached the stiffener. The experiment was performed under displacement control.

4.2. Modeling

A modeling approach, similar to that used in the DCB test simulation, was used to simulate the facesheet buckling and delamination propagation in the 914×914 mm (36×36 in.) debond panel. The cohesive model obtained from the DCB and FWT tests, and the mesh size calibrated from the DCB test simulation was used. The mode mixity of the facesheet buckling and delamination propagation may be different from the honeycomb DCB test. However, justifications for using the same cohesive model as in the DCB test simulation are:

– The buckling and delamination propagation in the honeycomb panel and the debond propagation in DCB are both Mode-I dominant.
– The buckling-driven delamination propagation between the facesheet and the honeycomb core due to the Mode-II and Mode-III contributions are taken into account by the mode-coupled cohesive model used in this study.

To simulate unstable crack growth with snap-back behavior within a framework of a static analysis approach, the arc-length control method can be used. However, the snap-back behavior due to the propagation of the debond front was so severe that a stable numerical solution

Table 4. Key parameters in analyses of debond panel

Case	σ_c (MPa (psi))	G_c (J/m^2 (lb/in.))	Damping (%)
Case 1	13.8 (2000)	788 (4.5)	0.001
Case 2	13.8 (2000)	788 (4.5)	1.000
Case 3	6.9 (1000)	525 (3.0)	1.000
Case 4	6.9 (1000)	788 (4.5)	1.000

could not be obtained with the static analysis. Instead, a transient analysis was performed to overcome the numerical problems of static analysis.

In the transient analysis, inertia and damping effects were considered. These effects stabilize the numerical solution process. The loading rate was calculated from the displacement loading rate in the experiment (0.318 mm/min (0.0125 in./min)) multiplied by the initial elastic stiffness of the debond panel. Since damping of the panel was not reported, the structural damping coefficients were assumed. Damping was selected based on the fact that the composite panels may have a substantial amount of damping and an assumption that the damping should not affect the overall response drastically.

The material properties were the same as those used in the DCB simulations. Values of $\sigma_c = 13.8$ MPa (2000 psi), $G_c = 788$ J/m^2 (4.5 lb/in.), and 0.001% Rayleigh damping were used in a baseline Case 1, Table 4. Parametric analyses were performed on the damping coefficient, G_c, and σ_c (Cases 2, 3 and 4, Table 4). Case 2 investigated the change in the crack propagation rate due to a larger damping coefficient. Cases 3 and 4 studied the sensitivity of the fracture parameters on the delamination propagation load. The analyses of Case 3 and 4 were performed with the same larger damping (1.0%) to obtain better numerical stability.

The finite element mesh is shown in Figure 17. A quarter of the whole panel was modeled considering symmetry of the panel (Figure 16b). As in the DCB simulation, top and bottom facesheets were modeled by four-noded shell elements. Eight-noded solid elements were used for the homogenized honeycomb core. Also, eight-noded 3D interface elements were used to represent the interface between the top facesheet and the homogenized core. To simulate the stiffeners a line of linear elastic interface elements with very high stiffness was assigned. The number of degrees of freedom for the model was 32 864. The Newmark-β implicit time integration method was used.

4.3. Results

In the 914×914 mm (36×36 in.) debond panel simulations, an eigenvalue analysis was performed before the facesheet buckling and delamination propagation analysis. The first eigenvector from the eigenvalue analysis was embedded as an initial imperfection in the panel so that a facesheet could buckle away from the honeycomb core during the delamination propagation analysis. The first two elastic buckling load and mode shapes from the eigenvalue analysis are shown in Figure 18. The first elastic buckling load was 182 kN (41 kips), which is similar to the value from an analytical approach and the experimental result (Boeing, 1996). The first mode, a half sine mode in the delamination area, was embedded into the panel geometry. The maximum magnitude of the imperfection was 0.254 mm (0.01 in.) (1% of the core thickness)

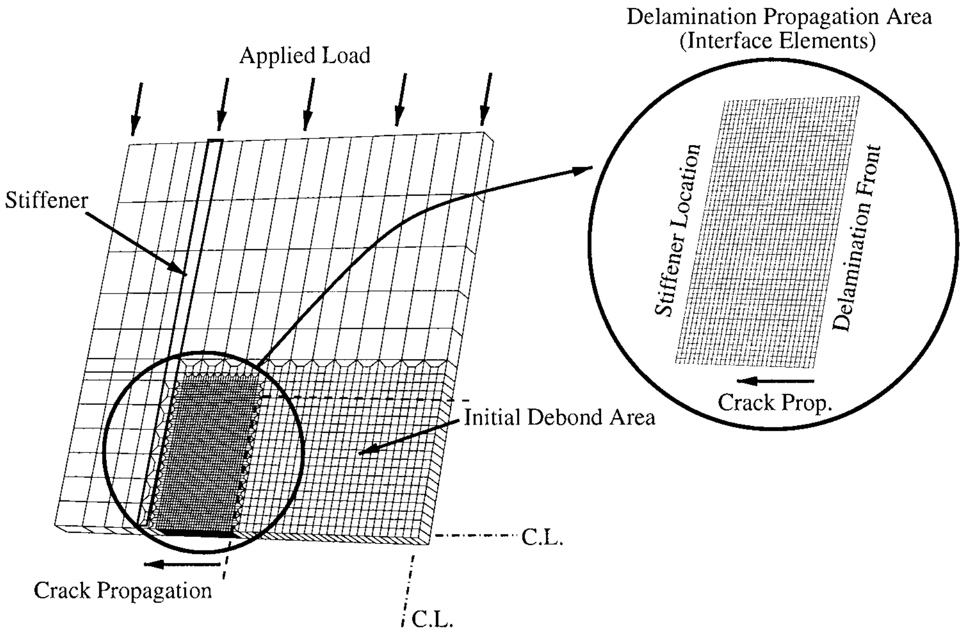

Figure 17. Honeycomb debond panel mesh (1/4 of 914×914 mm (36×36 in.) panel).

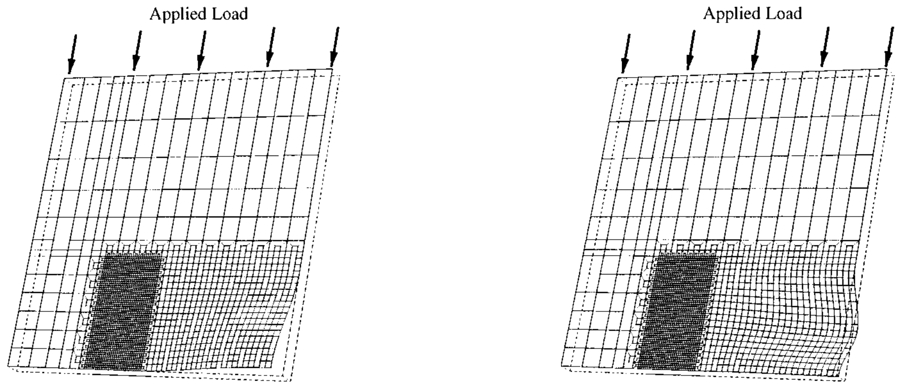

a. First mode ($P_{cr,I}$ = 182 kN (41 kips)) b. Second mode ($P_{cr,II}$ = 556 kN (125 kips))

Figure 18. Elastic buckling loads and mode shapes from eigenvalue analysis.

at the center of the actual debond area, which is the lower right corner in the finite element mesh shown in Figure 17.

The predicted in-plane loading versus in-plane displacement is plotted in Figure 19. The in-plane loading versus out-of-plane displacement at the center of the debond area is plotted in Figure 20. The deformed shapes and the crack front in the delamination propagation area at four load levels for Case 1 are shown in Figure 21.

Figure 19 shows that the in-plane initial stiffness in the simulation is slightly larger than in the experiment. This might be due to assumptions in the simulation model, i.e. the core homogenization, the isotropy assumption of the facesheet with bending stiffness, as well as uncertainties in the experiment. As the load increased the facesheet buckled away from the honeycomb core (Figure 20). As expected, the nonlinear buckling load with imperfection was lower than the ideal elastic buckling load. The predicted nonlinear buckling load (Figure 20)

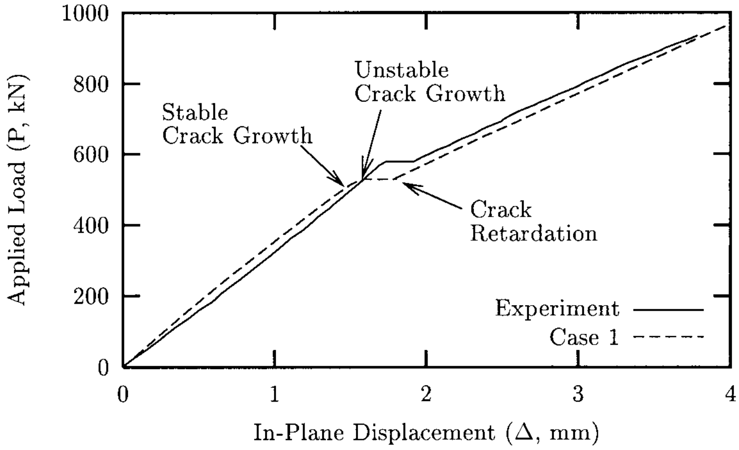

Figure 19. Applied load versus in-plane displacement (Case 1).

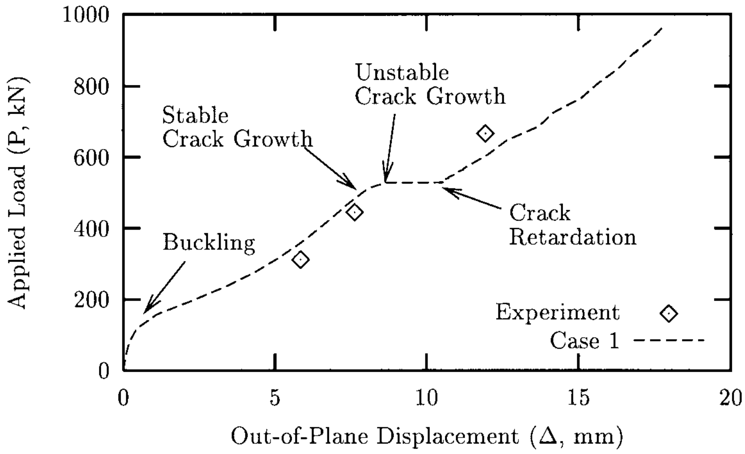

Figure 20. Applied load versus out-of-plane displacement (Case 1).

was slightly lower than the calculated elastic buckling load (182 kN (41 kips)). After buckling, the applied load increased by about a factor of three without delamination propagation.

The delamination first propagated in a stable fashion without much in-plane and out-of-plane stiffness change (from Figure 21a to Figure 21b). Significant in-plane and out-of-plane stiffness reduction is predicted as the crack begins to grow faster (Figures 19 and 20). The delamination propagation load which caused fast crack propagation was about 525 kN (118 kips). This is about 9% lower than the observed unstable delamination propagation load (578 kN (130 kips)). The discrepancy might be due to the assumptions in the simulation and uncertainties in the experiment. While the initial debond was ideal in the simulation model, the initial debond in the experiment could be behaving as a blunt notch rather than a sharp crack. The critical energy release rate for the cohesive model was determined from the DCB test results away from the initial notch to remove sawcut effects. This may have caused the under-prediction of the initial delamination propagation load when compared to the experiment.

The elapsed time during the unstable delamination process from simulation was about 9 ms. The time for unstable crack propagation from the experiment was not measured: It occurred between two frames of the video recording movie of the experiment. Therefore, it is certainly less than 30 ms, the frame period of the video recording of the experiment. It is concluded that the period of unstable crack propagation predicted from the simulation was on the same order of magnitude as the experiment.

Unstable delamination propagation was arrested by the line of the linear elastic interface elements with very high stiffness (the left edge of the fine mesh in Figure 21c). The crack growth direction then changed, and the crack propagated upward, opposite to the applied load direction (Figure 21d). In this fashion, 95.3 mm (3.75 in.) of the crack propagation from the initial delamination front to the stiffener could be simulated. After the delamination growth retardation, the honeycomb panel partially recovers its in-plane stiffness. The recovered stiffness from the simulation was similar to the experimental result (Figure 19).

In spite of the uncertainties both in the experiment and the simulation, it is concluded that the overall simulation predictions (pre- and post-buckling behavior, delamination propagation, and behavior after crack retardation) agree well with the experimental observations.

4.4. Sensitivity

This section describes the results of parametric analyses on the damping coefficient, G_c, and σ_c. An analysis with a different damping coefficient was performed (Case 2 in Table 4). Fracture parameters in Case 2 were the same as those in Case 1, but 1% damping was used instead of 0.001% damping. The simulation results for Case 1 and Case 2 were the same until the unstable delamination propagation load was reached. Although substantial stiffness decrease was predicted in Case 2, a finite positive slope was maintained during the delamination propagation (Figures 22 and 23). The elapsed time for the fast delamination process from Case 2 was about 5 s, which is significantly longer than that from Case 1 (9 ms), and the upper bound time from the experiment (30 ms). The crack propagation predicted from Case 2 is not a distinct unstable process as observed in the experiment. This is due to an overestimated damping coefficient. However, the difference in overall load versus displacement relationships between Case 1 and Case 2 is not significant. Therefore, 1% damping was used in subsequent parametric analyses (Case 3 and Case 4) for better numerical stability than the 0.001% damping.

To investigate the sensitivity of the stable/unstable delamination propagation load to G_c and σ_c, parametric analyses were performed. In Case 3, G_c was reduced to 525 J/m^2 (3.0 lb/in.) while other parameters were the same as those in Case 2. The unstable delamination propagation load was about 489 kN (110 kips) for $G_c = 525$ J/m^2 (3.0 lb/in.) (Figure 24). This is about 15% lower than the observed delamination propagation load (578 kN (130 kips)) from the experiment, and about 7% lower than the propagation load (525 kN (118 kips)) for $G_c = 788$ J/m^2 (4.5 lb/in.) (Case 2). In Case 4, σ_c was reduced to 6.9 MPa (1000 psi). The unstable delamination propagation load from Case 4 is at most 1% lower than the propagation load from Case 2 (Figure 25). Similar to the DCB simulation results, the delamination propagation load is dominated by G_c rather than σ_c.

5. Conclusions

The feasibility of applying the cohesive crack propagation model as a method to simulate delamination propagation between a facesheet and a core in a honeycomb panel was investigated. Experiments were performed to measure the two key parameters of the cohesive model. The G_c value was determined from the DCB tests, and σ_c was selected from FWT test

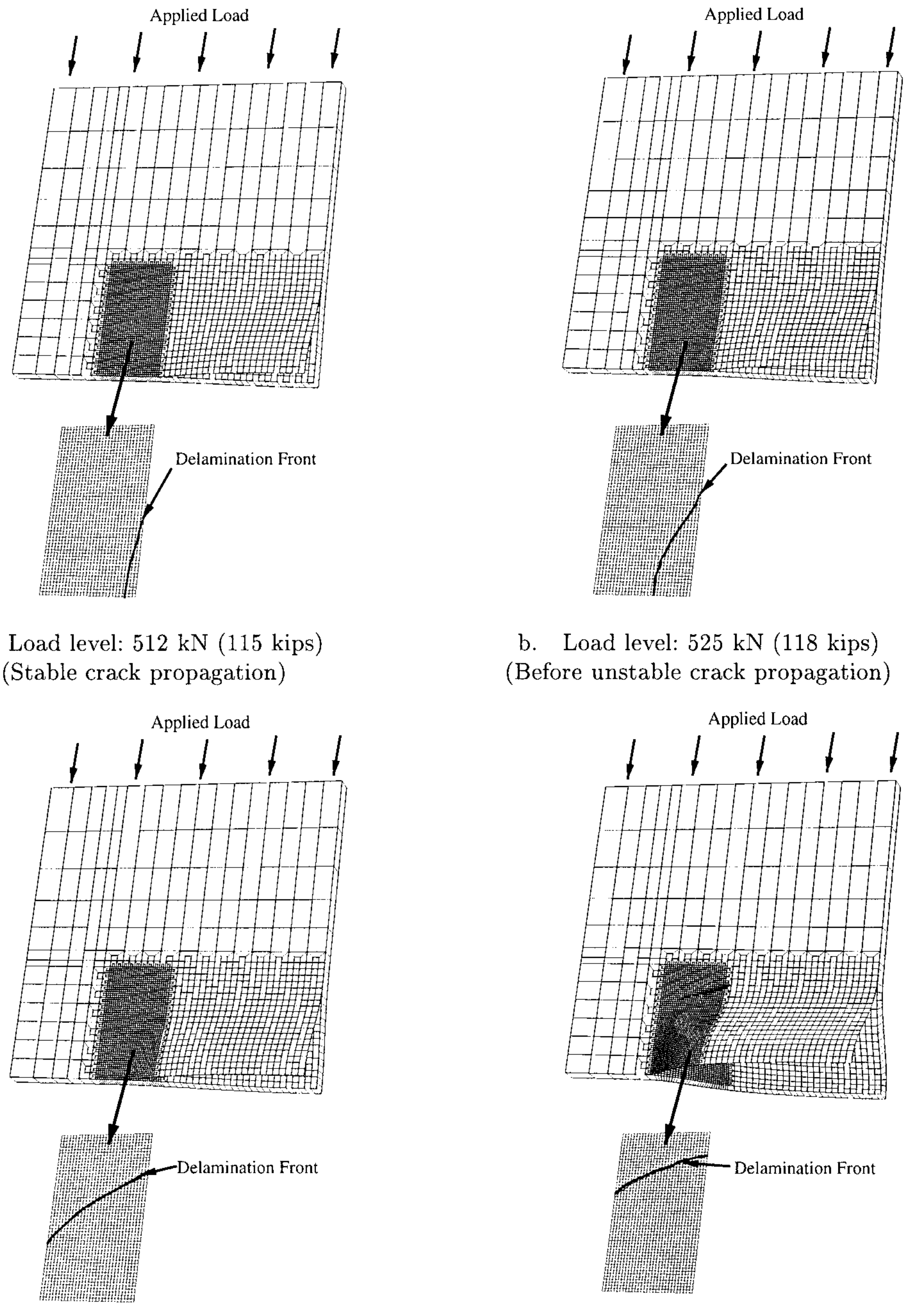

a. Load level: 512 kN (115 kips)
(Stable crack propagation)

b. Load level: 525 kN (118 kips)
(Before unstable crack propagation)

c. Load level: 525 kN (118 kips)
(After unstable crack propagation)

d. Load level: 890 kN (200 kips)
(After crack retardation by stiffener)

Figure 21. Deformed shapes of honeycomb panel and crack front in delamination area (Case 1; magnification factor for deformed shape = 4).

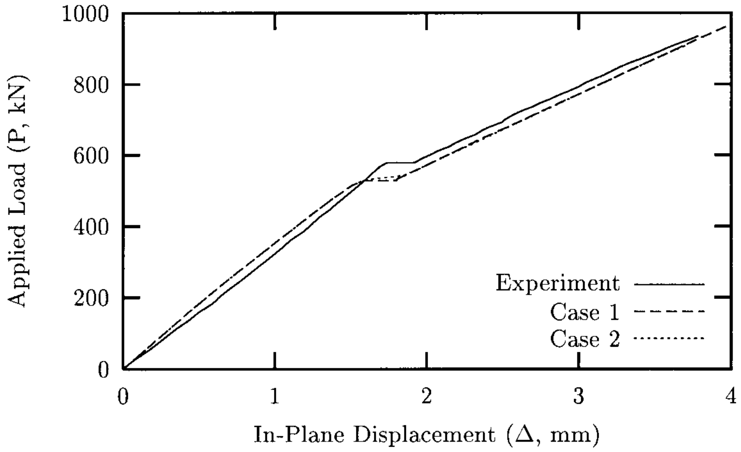

Figure 22. Applied load versus in-plane displacement. Comparison between Case 1 and Case 2 (damping).

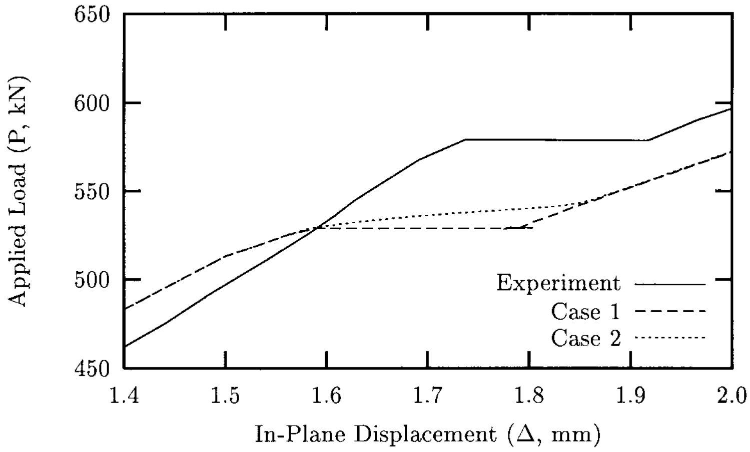

Figure 23. Applied load verses in-plane displacement. Comparison between Case 1 and Case 2 (damping). Zoomed around unstable crack growth region.

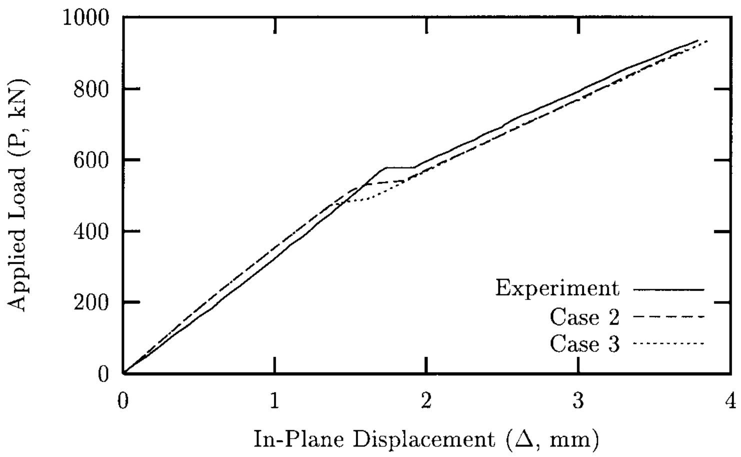

Figure 24. Applied load versus in-plane displacement. Comparison between Case 2 and Case 3 (G_c).

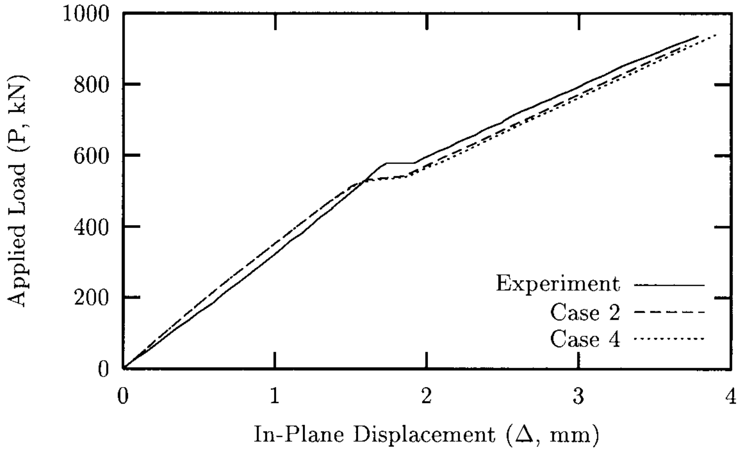

Figure 25. Applied load versus in-plane displacement. Comparison between Case 2 and Case 4 (σ_c).

results. To reduce the computational cost, core homogenization was performed and both the facesheets and the core were modeled as linear elastic materials. The fracture process between the facesheet and the core was modeled using cohesive interface elements.

The DCB simulation was successfully performed within crack lengths from 50.8 mm (2 in.) to 102 mm (4 in.) where G_c was measured. The parametric study on σ_c for the cohesive model showed that the cohesive zone length decreases as σ_c increases, but the mathematical crack front paths remain unchanged. The parametric study on G_c showed that G_c is the sensitive parameter which determines the delamination load for crack propagation. The results were mesh-insensitive if at least one or two interface elements were inside the cohesive zone. These parametric studies suggest that the fracture-mechanics-based approach should be used in a delamination propagation analysis of a honeycomb panel as opposed to a strength-based approach.

The overall response of the 914×914 mm (36×36 in.) debond panel simulation results captured the dominant behavior observed in the experiment in spite of the absence of precise information on the loading rate and damping of the panel. The 9% under-prediction of the unstable delamination propagation load, which is conservative compared with the experimental result, can be considered accessible for practical purposes. The stable/unstable crack growth simulation was successfully performed, and the change of delamination growth direction after crack retardation by the stiffener was also simulated.

It is concluded that the cohesive element approach allows successful simulation of a facesheet buckling and delamination propagation problem between a facesheet and a core in a realistic honeycomb panel. The current task can also be considered as a guide for simulating debonding between a facesheet and a core in a honeycomb panel using the cohesive element approach. The debonding process of a realistic honeycomb panel can be simulated by first measuring the dominant parameter, G_c and σ_c from DCB and FWT tests, respectively, and then applying the determined cohesive model to the realistic structure.

Acknowledgements

The calculations have been carried out with the finite element program DIANA of TNO Building and Construction Research, the Netherlands. This research was supported by the Boeing Commercial Airplane Company, by the Multidisciplinary Center for Earthquake Engineering Research, and by Cornell University. The authors gratefully acknowledge the contributions of Dr. Peter H. Feenstra, Prof. Chung-Yuen Hui, and Dr. Paul A. Wawrzynek at Cornell University.

References

Barenblatt, G.I. (1962). The mathematical theory of equilibrium cracks in brittle fracture. *Advances in Applied Mechanics* **VII**, 55–129.

Boeing (1996). *Structural Material Laboratory Work Request*. Technical report, Boeing HSCT Structures Technology. Unpublished.

Burton, W.S. and Noor, A.K. (1997). Assessment of continuum models for sandwich panel honeycomb cores. *Computer Methods in Applied Mechanics and Engineering* **145**, 341–360.

Chai, H., Babcock, C.A. and Knauss, W.G. (1981). One dimensional modeling of failure in laminated plates by delamination buckling. *International Journal of Solids and Structures* **17**, 403–426.

Cui, W. and Wisnom, M.R. (1993). A combined stress-based and fracture-mechanics-based model for predicting delamination in composites. *Composites* **24**, 467–474.

de Andres, A., Perez, J.L. and Ortiz, M. (1999). Elastoplastic finite element analysis of three-dimensional fatigue crack growth in aluminum shafts subjected to axial loading. *International Journal of Solids and Structures* **36**, 2231–2258.

Dugdale, D.S. (1960). Yielding in steel sheets containing slits. *Journal of the Mechanics and Physics of Solids* **8**, 100–104.

Kim, W., Miller, T. and Dharan, C. (1981). Strength of composite sandwich panels containing debonds. *International Journal of Solids and Structures* **30**, 211–223.

Klug, J., Wu, X.X. and Sun, C.T. (1996). Efficient modeling of postbuckling delamination growth in composite laminates using plate elements. *AIAA Journal* **34**, 178–184.

Miller, M., Rufin, A.C., Westre, W.N. and Samavedam, G. (1998). High-speed civil transport hybrid laminate sandwich fuselage panel test. In: *Fatigue and Fracture Mechanics* (edited by Panonthin T. and Sheppard S.), Vol. 29, ASTM STP 1321, 713–726.

Nilsson, K.-F. and Giannakopoulos, A.E. (1995). A finite element analysis of configurational stability and finite growth of buckling driven delamination. *Journal of the Mechanics and Physics of Solids* **43**, 1983–2021.

Nilsson, K.-F. and Storakers, B. (1992). On interface crack growth in composite plates. *Journal of Applied Mechanics* **59**, 530–538.

Nilsson, K.-F., Thesken, J.C., Sindelar, P., Giannakopoulos, A.E. and Storakers, B. (1993). A theoretical and experimental investigation of buckling induced delamination growth. *Journal of the Mechanics and Physics of Solids* **41**, 749–782.

Ortiz, M. and Pandolfi, A. (1999). Finite-deformation irreversible cohesive elements for three-dimensional crack-propagation analysis. *International Journal for Numerical Methods in Engineering* **44**, 1267–1282.

Rice, J.R. (1968). Mathematical analysis in the mechanics of fracture. In: *Fracture: An Advanced Treatise* (edited by Liebowitz, H.), Academic Press, New York, 191–311.

Schellekens, J.C.J. and de Borst, R. (1993). On the numerical integrations of interface elements. *International Journal for Numerical Methods in Engineering* **36**, 43–66.

Tsai, S.W. (1987). *Composites Design*. Dayton: Think Composites, third edition.

Ural, A., Zehnder, A.T. and Ingraffea, A.R. (2001). Fracture mechanics approach to facesheet delamination in honeycomb: Measurement of energy release rate of the adhesive bond. *Engineering Fracture Mechanics*. (submitted).

Wei, Y. and Hutchinson, J.W. (1997). Steady-state crack growth and work of fracture for solids characterized by strain gradient plasticity. *Journal of the Mechanics and Physics of Solids* **45**, 1253–1273.

Whitcomb, J.D. (1981). Finite element analysis of instability related delamination growth. *Journal of Composite Materials* **15**, 403–426.

Whitcomb, J.D. (1989). Three-dimensional analysis of a postbuckled embedded delamination. *Journal of Composite Materials* **23**, 862–889.

Whitcomb, J.D. (1992). Analysis of a laminate with a postbuckled embedded delamination. *Journal of Composite Materials* **26**, 1523–1533.

Wilhite, A.W. and Shaw, R.J. (1997). HSCT research picks up speed. *Aerospace America* **35**, 24–29,41.

Williams, L.J. (1995). HSCT research gathers speed. *Aerospace America* **145**, 32–37.